

#### Contents lists available at ScienceDirect

# Energy

journal homepage: www.elsevier.com/locate/energy



# A self-floating oscillating surge wave energy converter

Qiaofeng Li, Jia Mi, Xiaofan Li, Shuo Chen, Boxi Jiang, Lei Zuo\*

Department of Mechanical Engineering, Virginia Tech, 1145 Perry St., Blacksburg, VA, 24061, USA



#### ARTICLE INFO

Article history: Received 26 October 2020 Received in revised form 3 March 2021 Accepted 12 April 2021 Available online 3 May 2021

Keywords: Wave energy converter Self-floating Oscillating surge device Energy harvesting Marine energy

#### ABSTRACT

This paper proposes a new conceptual configuration for oscillating surge wave energy converters. The concept is a self-floating device consisting of two vertical flaps with a common hinge and an averaged density equal to that of water. The two flaps will oscillate in opposite directions when driven by incident waves. Kinetic energy will be extracted from the relative speed between the two flaps by a power take-off embedded at the hinge. Numerical studies reveal that the self-floating device has a smaller resonant period and optimal power take-off damping compared with a bottom-hinged floating device of the same overall dimensions. As long as the power take-off damping is appropriately tuned, the opposite-rotation mechanism is valid in both regular and irregular waves, and no matter whether the hinge is fixed or connected with mooring lines. With the self-floating feature and opposite-rotation mechanism, the proposed concept can potentially benefit deep ocean applications by exerting a significantly less reaction loading on mooring lines and eliminating the need for a supporting frame to house the power take-off. The influence of various design parameters such as flap dimensions, submerged depth, incident wave direction, and water depth is also analyzed for a comprehensive evaluation of the proposed concept.

© 2021 Elsevier Ltd. All rights reserved.

## 1. Introduction

The ocean reserves a tremendous amount of untapped renewable energy in the form of wave, current, temperature (thermal) and salinity gradients. The global wave energy potential is estimated to be  $8000 \sim 80,000$  TWh/y [1]. In fact, the wave energy is 4–5 times larger than the ocean energy in the rest of the forms combined. Wave energy possesses a high energy density, e.g. rated at 25 kW/m² at San Francisco coast [2]. The great potential of wave energy has attracted enormous attention from academia, industry, and government [3]. For example, the UK has declared wave energy as an essential component to its net zero 2050 goal and projected the creation of 8100 new high value jobs in this sector by 2040 [4].

A variety of forms of machinery, collectively named wave energy converters (WEC), have been developed to convert wave kinetic energy into electricity or pressure energy [5]. These machinery can be categorized into oscillating water columns, overtopping devices, and wave activated bodies according to their working principles. Oscillating water columns use pneumatic pressure variation in a partially submerged chamber to drive a turbine and then a generator for electricity. In the submerged chamber, alternate pneumatic

breakwaters [11].

Wave activated bodies encompass a significant portion of research and commercial efforts in the field [12]. Wave activated bodies use the relative motion between a body and the seabed or between multiple bodies to generate energy. The relative motion can be essentially translational or rotational. The Pelamis [13] WEC consists of a set of semi-submerged cylinders jointed by hinges. Upon the incident waves, different sections of the WEC would generate motions of different orientations in different phases. The relative rotational movement is converted into electricity by the hydraulic power take-offs (PTOs) inside the hinges. Stansby et al.

[14-16] proposed the multi-float multi-mode-motion (M4) wave

air compression and decompression will occur in response to incident waves. The air will flow through pipes and valves into a

ducted turbine [6] and drive the generator. Oscillating water col-

umns can be installed onshore, integrated with breakwaters [7], or

deployed afloat/offshore for larger energy input [8,9]. Overtopping

devices typically consist of a ramp and a reservoir. The incident

waves would overtop the ramp and enter the reservoir. The stored water will flow through controlled gates and low head turbines to

generate electricity, and finally back to the ocean. The generated

energy comes from the potential energy difference between the

water stored in the reservoir and at the mean water surface, which

eventually originates from the kinetic energy in the incident waves.

Overtopping devices can also be floating [10] or integrated into

E-mail address: leizuo@vt.edu (L. Zuo).

<sup>\*</sup> Corresponding author.

energy converter, as a significant improvement to previous attenuators. The M4 WEC consists of three segments of in-line floats increasing in diameter and number from bow to stern so that the device heads into the incoming wave direction naturally. The PTO at the hinge point above the mid float harvests energy from the relative motion between the stern float and the rigid sub-assembly of bow and mid floats. Beatty et al. [17] studied the influence of the geometry of the second body in self-reacting point absorbers. Two geometries are compared: a tank and a heave plate. The conclusion is that the natural frequency of the point absorber with a tank is higher due to the comparably small added mass. Liang et al. [18] designed a rack and pinion-based mechanical motion rectifier (MMR) PTO and tested its performance on a single-body heaving point absorber. The heaving motion of the point absorber is converted into uni-directional rotation of a DC generator through two sets of rack pinions and one-way bearings. Li et al. [19,20] proposed harvesting the wave energy from the relative motion between two bodies of a self-reactive WEC using a ballscrew-based MMR PTO. The bidirectional relative translational motion between the two bodies is first converted into bidirectional rotation of a ballscrew and then into the uni-directional rotation of a generator through two one-way clutches in the MMR gearbox. Extensive literature can be found on hydrodynamic configuration and performance [21–25], PTO mechanisms [26–30], and control strategies [31–34].

Oscillating surge wave energy converters (OSWECs, also referred to as oscillating wave surge converters) are among the popular forms of WECs [12]. The initial form of OSWEC is a huge buoyant flap hinged at the seabed in nearshore coastal zone. Driven by the horizontal fluid movement of waves, the flap will oscillate in surge motion and rotate with respect to the bottom hinge. Kinetic energy is converted from the relative rotation between the flap and a fixed frame typically with hydraulic pumps. Whittaker and Folley [35] brought forward the Oyster OSWEC idea, which is one of the earliest efforts on the development of OSWEC and resulted in Oyster 800, a device rated at 800 kW and deployed 500 m from the coast of Orkney at EMEC in a water depth of approximately 13 m. Devices based on similar principles include WaveRoller [36,37] and Resolute Marine device [38,39]. Sarkar et al. [40] have exploited the hydrodynamics of the modular concept of OSWEC. A traditional OSWEC flap is divided into several segments with their own Degrees of Freedom (DoFs). It is shown that due to the occurrence of multiple resonances, the modular concept captures more energy at higher wave periods than traditional design. Tom et al. [41] proposed an adaptive OSWEC concept with control surfaces. The control surfaces enable a variable geometry that modifies the hydrodynamics properties of the system according to external conditions. Results show that when transitioning from moderate to large ocean states, the variable geometry concept can reduce the structural loads and maintain the power generation. Ruehl et al. [42] developed and tested a floating OSWEC (FOSWEC) in wave basin. The FOSWEC is consisted of a floating platform and two pitching flaps. The energy is extracted through relative motion between the pitching flaps and the platform. Although the development of OSWECs is active, the majority of applications is still restricted to shallow waters. Deep water sites are favoured for OSWEC deployments because of the near shore permitting issues and the abundant offshore wave resources [43]. The prototype in Ref. [42] targets at deep water deployments. However, additional hazards exist when the large flaps of a scaled-up device rotate violently in an energetic ocean environment and exert a huge loading on the mooring systems. Studies have demonstrated with consent that the general OSWEC design is subject to large hydrodynamic loads that drive the material cost [44]. Maximizing energy generation while minimizing structural loadings is an essential step for reliable operations of OSWECs in deep water, and in general for advancing wave energy technologies towards commercial viability [41,45].

In this paper, we propose the self-floating OSWEC (SF-OSWEC), to solve the above problem and as a complement to the exploration efforts of OSWEC variants. The concept and its potential applications are illustrated in Fig. 1. The SF-OSWEC is consisted of two flaps of the same dimensions, one with a density smaller than seawater and the other one larger. The two flaps share a common hinge where the mooring lines are connected. The two flaps have an averaged density equal to seawater, so the mooring lines are not forced in static states (except some prestress in practical applications) and experience less loading in dynamic working conditions. Driven by incident waves, the two flaps will rotate in opposite directions and phases. The opposite motion will be picked up by a PTO system embedded at the hinge, such as a generator with its stator connected with the bottom flap and rotor connected with the top flap. The equivalent rotation speed of the PTO is the summation of the pitching speeds of the two flaps. In this way, the energy from the two flaps is extracted and synthesized. In this paper, we will introduce the detailed modelling method of this SF-OSWEC concept, reveal its operating principles, and establish the difference between the SF-OSWEC and traditional bottom-hinged floating OSWEC (BH-FOSWEC) of the same overall dimensions. The goal is not to definitely conclude a better concept since the authors believe different concetps/devices have their own advantages and optimal application scenarios. A comprehensive evaluation will be presented on the influence of different design parameters on the SF-OSWEC performance, such as mooring line stiffness, flap width, height, density, submerged depth, incident wave direction, and water depth. It is worth mentioning the significant difference between the floating device in Ref. [42] and the proposed SF-OSWEC. The former adopts two buoyant flaps connected with the same supporting frame. The energy is extracted by PTOs from the relative motion between the frame and each flap. The proposed SF-OSWEC consists of one buoyant flap and one gravity flap. The energy is directly extracted from the relative motion between the two flaps and no supporting frame is needed.

The paper is organized in 3 sections as follows. Section 2 introduces the time domain dynamic models for both with and without moorings cases. Section 3 studied the differences between SF-OSWEC and BH-FOSWEC and the unique properties of SF-OSWEC in detail. The influence of different design parameters, such as mooring stiffness, submerged depth, flap height, incident wave direction, and so on, on the performance of SF-OSWEC is also investigated to comprehensively characterize the device. Section 4 concludes the research.

#### 2. Problem formulation

In this section, we establish the governing equations for the self-floating oscillating surge wave energy converter (SF-OSWEC). We will first establish the time domain dynamic model for SF-OSWEC without mooring in order to exaggerate the difference between SF-OSWEC and traditional bottom-hinged floating OSWEC (BH-FOSWEC). Then we incorporate mooring into the dynamic model, which is represented by horizontal and vertical springs with large stiffness values, in order to demonstrate the performance of SF-OSWEC under a more realistic and comprehensive settings. We comment on the relationship between these two models and their limitations in the end.

## 2.1. Without mooring

The coordinate system and dimensions of SF-OSWEC are shown

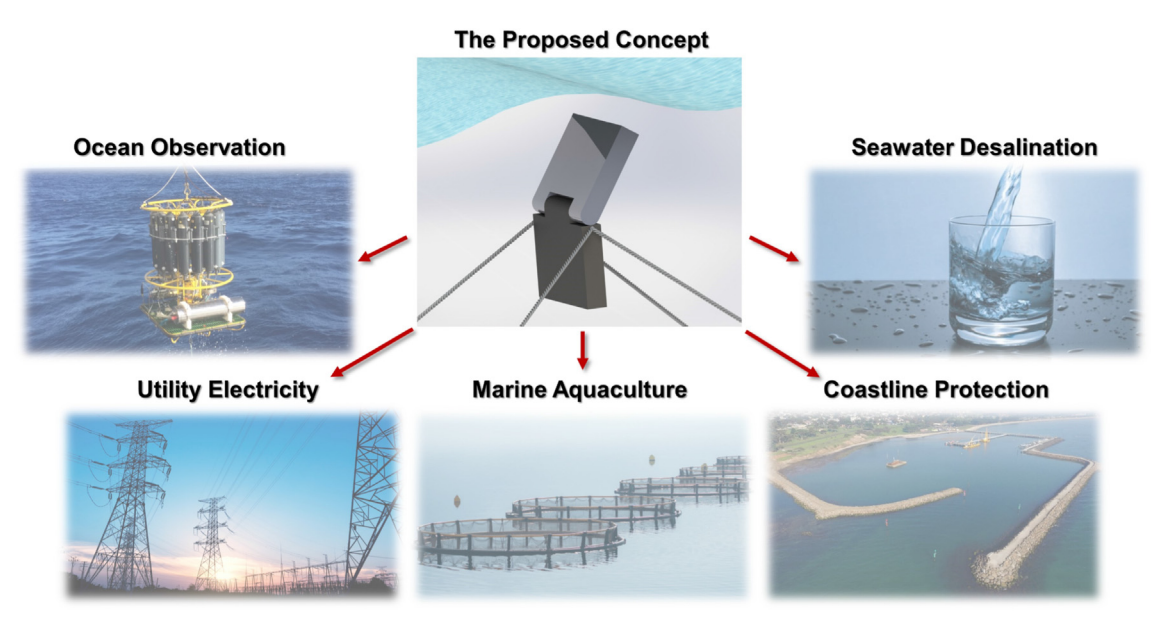


Fig. 1. Potential applications of the proposed SF-OSWEC concept.

in Fig. 2. The wave direction is the *x*-axis direction, and the device is positioned symmetrically to YOZ and XOZ planes. Although the hydrodynamics of the device will be calculated in 3D in the following, the multi-body dynamics of the system is only considered in the XOZ plane, i.e., only surge, heave, and pitch motions are considered. The governing equations for the SF-OSWEC without mooring lines are

$$(\mathbf{M} + \mathbf{A}_{\infty})\dot{\mathbf{y}} + \mathbf{C}\dot{\mathbf{y}} + \mathbf{K}\mathbf{y} = \mathbf{F}_{exc} + \mathbf{F}_{prad} + \mathbf{F}_{buov} + \mathbf{D}_{1}^{T}\lambda$$
 (1)

where  $\mathbf{y} \in \mathbb{R}^{6 \times 1}$  is the vector of the system Degrees of Freedom (DoFs),

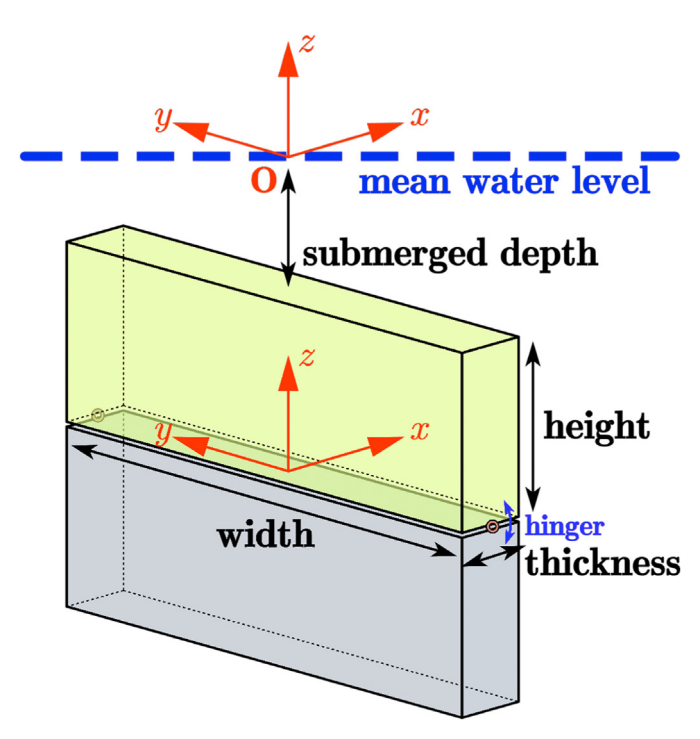


Fig. 2. The dimension parameters of SF-OSWEC.

$$\mathbf{y} = \begin{bmatrix} x_1 & z_1 & \theta_1 & x_2 & z_2 & \theta_2 \end{bmatrix}^{\mathrm{T}} \tag{2}$$

where  $x_i$ ,  $z_i$ , and  $\theta_i$  (i=1,2) represent the surge, heave, and pitch motion of the *i*th-body (at the center of mass). i=1 corresponds to top flap and i=2 the bottom flap. **M** is the system mass matrix,

$$\mathbf{M} = \begin{bmatrix} \mathbf{M}_1 & \\ & \mathbf{M}_2 \end{bmatrix} \tag{3}$$

where

$$\mathbf{M}_{i} = \begin{bmatrix} m_{i} & \\ & m_{i} \\ & J_{i} \end{bmatrix} (i = 1, 2) \tag{4}$$

where  $m_i$  is the mass of the ith flap, and  $J_i$  is the moment of inertia of the ith flap with respect to its center of mass. In this paper we assume uniform densities for the flaps, so the center of mass is the center of geometry.  $\mathbf{A}_{\infty}$  is the added mass matrix for the system at the infinite frequency.

$$\mathbf{A}_{\infty} = \begin{bmatrix} \mathbf{A}_{1,1} & \mathbf{A}_{1,2} \\ \mathbf{A}_{2,1} & \mathbf{A}_{2,2} \end{bmatrix} \tag{5}$$

 $\mathbf{A}_{i,j}$  represents the added matrix between the ith body and jth body. If  $i \neq j$ , it represents the interaction between ith and jth body.  $\mathbf{C}$  is the system damping matrix.

$$\mathbf{C} = \begin{bmatrix} \mathbf{0}_{2\times2} & \mathbf{0}_{2\times4} \\ & c_{pto} & \cdots & -c_{pto} \\ \mathbf{0}_{4\times2} & \vdots & & \vdots \\ & -c_{pto} & \cdots & c_{pto} \end{bmatrix}$$
(6)

where  $c_{pto}$  is the PTO damping coefficient. The static buoyancy force on the system is represented as

$$\mathbf{F}_{buoy} \in \mathbb{R}^{6 \times 1} = \begin{bmatrix} 0 & (\rho_{water} - \rho_1) g V_1 & 0 \\ 0 & (\rho_{water} - \rho_2) g V_2 & 0 \end{bmatrix}^{\mathrm{T}}$$

$$(7)$$

where  $\rho_{water}$  is the density of water,  $\rho_i$  is the density of the ith body,  $V_i$  is the volume of the ith body, and g is the gravity acceleration.  $\mathbf{F}_{prad} \in \mathbb{R}^{6 \times 1}$  is the radiation damping force excluding the added mass effect (they are already considered in the system mass), where its ith component is (the Cummins equation [46])

$$\mathbf{F}_{prad,i} = -\sum_{j=1}^{6} \int_{0}^{t} K_{ij}(t-\tau)\dot{y}_{j}(\tau)d\tau$$
(8)

where  $\dot{y}_j(t)$  is the jth component of  $\dot{\mathbf{y}}$  at time instant t. is the impulse response function of ith DoF with respect to the jth DoF,

$$K_{ij}(t) = \frac{2}{\pi} \int_{0}^{\infty} B_{ij}(\omega) \cos(\omega t) d\omega$$
 (9)

 $B_{ij}(\omega)$  is the coupled radiation damping coefficient between the *i*th and *j*th DoFs at angular frequency  $\omega$ .  $\mathbf{F}_{exc}(t)$  is the wave excitation force, and in regular wave conditions is represented as

$$\mathbf{F}_{exc}(t) = \mathcal{R}\left[\frac{H}{2}\mathbf{F}_{exc}(\omega)e^{i\omega t}\right]$$
 (10)

where  $\mathbf{F}_{exc}(\omega) \in \mathbb{R}^{6 \times 1}$  is the complex excitation force vector at excitation frequency  $\omega$ . H is the wave height.  $\mathscr{R}[\, {}^{\star}]$  is the real part of a complex number. In irregular wave conditions, it should be

$$\mathbf{F}_{exc}(t) = \mathcal{R} \left[ \sum_{j=1}^{N_{\omega}} \mathbf{F}_{exc}(\omega_j, \theta) e^{i(\omega_j t + \varphi_j)} \sqrt{2S(\omega_j) d\omega_j} \right]$$
(11)

where  $N_{\omega}$  is the number of frequency lines considered;  $\varphi_j$  is the random phase at  $\omega_j$ ;  $S(\omega)$  represents the wave spectrum.

 $\mathbf{D}_1 \in \mathbb{R}^{n_c \times 6}$  is the Jacobian matrix of the system constratins.  $n_c = 4$  is the number of constraints. For SF-OSWEC in fixed hinge conditions, we have 4 constraints

$$\begin{aligned} x_1 - \frac{l_1}{2}\sin\theta_1 &= 0 \\ z_1 + \frac{l_1}{2}(1 - \cos\theta_1) &= 0 \\ x_2 + \frac{l_2}{2}\sin\theta_2 &= 0 \\ z_2 - \frac{l_2}{2}(1 - \cos\theta_2) &= 0 \end{aligned}$$
 (12)

In this case  $\mathbf{D}_1$  is

$$\mathbf{D}_{1} = \begin{bmatrix} 1 & 0 & -\frac{l_{1}}{2}\cos\theta_{1} \\ 0 & 1 & \frac{l_{1}}{2}\sin\theta_{1} \end{bmatrix} \\ \begin{bmatrix} 1 & 0 & \frac{l_{2}}{2}\cos\theta_{2} \\ 0 & 1 & -\frac{l_{2}}{2}\sin\theta_{2} \end{bmatrix} \end{bmatrix}$$
(13)

where  $l_1$  and  $l_2$  are the heights of the top and bottom flaps respectively.

 $\lambda \in \mathbb{R}^{n_c \times 1}$  is the Lagrange multiplier. By differentiating the constraints Eq. (12) twice, we have the additional constraint equations

$$\mathbf{D}_{1}\ddot{\mathbf{y}} = \mathbf{F}_{c1} \in \mathbb{R}^{4 \times 1} = \begin{bmatrix} -\frac{l_{1}}{2}\sin\theta_{1} \cdot (\dot{\theta_{1}})^{2} & -\frac{l_{1}}{2}\cos\theta_{1} \cdot (\dot{\theta_{1}})^{2} \\ \frac{l_{2}}{2}\sin\theta_{2} \cdot (\dot{\theta_{2}})^{2} \frac{l_{2}}{2}\cos\theta_{2} \cdot (\dot{\theta_{2}})^{2} \end{bmatrix}^{T}$$

$$(14)$$

By combining Eqs. (1) and (14), we have the overall system governing equations as

$$\begin{bmatrix} \overline{\mathbf{M}} & -\mathbf{D}_{1}^{\mathrm{T}} \\ \mathbf{D}_{1} & 0 \end{bmatrix} \begin{bmatrix} \ddot{\mathbf{y}} \\ \lambda \end{bmatrix} = \begin{bmatrix} \overline{\mathbf{h}} \\ \mathbf{F}_{c1} \end{bmatrix}$$
 (15)

where

$$\overline{\mathbf{M}} = \mathbf{M} + \mathbf{A}_{\infty} \tag{16}$$

and

$$\overline{\mathbf{h}} = \mathbf{F}_{exc} + \mathbf{F}_{prad} + \mathbf{F}_{buoy} - \mathbf{C}\dot{\mathbf{y}} - \mathbf{K}\mathbf{y}$$
 (17)

By solving Eq. (15), we will have the system responses and reaction force histories from the constraints.

### 2.2. With mooring

With mooring lines the system governing equations should be refined as

$$(\mathbf{M} + \mathbf{A}_{\infty})\ddot{\mathbf{y}} + \mathbf{C}\dot{\mathbf{y}} + \mathbf{K}\mathbf{y} = \mathbf{F}_{exc} + \mathbf{F}_{mooring} + \mathbf{F}_{prad} + \mathbf{F}_{buoy} + \mathbf{D}_{2}^{\mathsf{T}}\lambda$$
 (18)

Compared to Eq. (1), an additional term  $\mathbf{F}_{mooring}$  has been added.

$$\mathbf{F}_{mooring} = \begin{bmatrix} -k_{mx} \left( x_1 - \frac{l_1}{2} \sin \theta_1 \right) \\ -k_{mz} \left( z_1 + \frac{l_1}{2} (1 - \cos \theta_1) \right) \\ k_{mx} \left( x_1 - \frac{l_1}{2} \sin \theta_1 \right) \frac{l_1}{2} \cos \theta_1 \\ -k_{mz} \left( z_1 + \frac{l_1}{2} (1 - \cos \theta_1) \right) \frac{l_1}{2} \sin \theta_1 \end{bmatrix}$$

$$\mathbf{0}_{3 \times 1}$$
(19)

where  $k_{mx}$  and  $k_{mz}$  are the mooring stiffness in the x and z directions. We have two constraints for the two flaps of SF-OSWEC with moorings

$$x_{1} - \frac{l_{1}}{2}\sin\theta_{1} = x_{2} + \frac{l_{2}}{2}\sin\theta_{2}$$

$$z_{1} + \frac{l_{1}}{2}(1 - \cos\theta_{1}) = z_{2} - \frac{l_{2}}{2}(1 - \cos\theta_{2})$$
(20)

We assemble the multi-body dynamics model by: (1) attaching the moorings to the top flap at the hinge location, which is enforced by Eq. (19); (2) attaching the top and bottom flaps to a common hinge, which is enforced by Eq. (20). By differentiating the constraint equations Eq. (20) twice, we have

$$\mathbf{D}_{2}\ddot{\mathbf{y}} = \mathbf{F}_{c2} \in \mathbb{R}^{2 \times 1} = \begin{bmatrix} -\frac{l_{1}}{2} \sin \theta_{1} \cdot (\dot{\theta_{1}})^{2} - \frac{l_{2}}{2} \sin \theta_{2} \cdot (\dot{\theta_{2}})^{2} \\ -\frac{l_{1}}{2} \cos \theta_{1} \cdot (\dot{\theta_{1}})^{2} - \frac{l_{2}}{2} \cos \theta_{2} \cdot (\dot{\theta_{2}})^{2} \end{bmatrix}^{T}$$
(21)

By combining Eqs. (18) and (21), we have the overall system governing equations as

$$\begin{bmatrix} \overline{\mathbf{M}} & -\mathbf{D}_{2}^{\mathrm{T}} \\ \mathbf{D}_{2} & 0 \end{bmatrix} \begin{bmatrix} \ddot{\mathbf{y}} \\ \lambda \end{bmatrix} = \begin{bmatrix} \overline{\mathbf{h}} \\ \mathbf{F}_{c2} \end{bmatrix}$$
 (22)

#### 2.3. The relationship between models with and without mooring

From Eq. (19), when the mooring lines are infinitely stiff, i.e.,  $k_{mx}$ ,  $k_{mz} \rightarrow \infty$ , to hold the first two terms of  $\mathbf{F}_{mooring}$  bounded, we have

$$x_1 - \frac{l_1}{2}\sin\theta_1 = 0$$

$$z_1 + \frac{l_1}{2}(1 - \cos\theta_1) = 0$$
(23)

Combining Eq. (23) with Eq. (20), we get Eq. (12). That is to say, the dynamic model of SF-OSWEC without moorings is equivalent to that of SF-OSWEC with infinite stiffness moorings.

#### 2.4. Model limitations

It should be noted that the following numerical results are based on (and somehow limited because of) several assumptions. This paper models the fluid-structure interaction based on the linear potential flow theory, and will inherit all the limitations originating from this theory, including ignoring drag forces on sharp edges, which may cause power capture to be significantly overestimated. This paper mainly focuses on demonstrating the difference in operating principles between the proposed and traditional devices, so some parameters/considerations necessary in practical design are ignored. The PTO system is simplified as a damping term in the above models. For the mooring lines, their inertia is ignored. They are simplified as mass-less springs in the dynamic models. The geometric interference between the two flaps of SF-OSWEC is also ignored. In practice, a clearance between the flaps should be determined based on the working rotation range, the flap dimensions, and the hinge design.

## 3. Numerical study

In this section, we study the dynamics of SF-OSWEC under different parameters, and make comparisons to the traditional BH-FOSWEC. In Section 3.1, we reveal the essential difference in operating principles of SF-OSWEC and BH-FOSWEC, with the assumption that the hinges are fixed (x and z coordinates). Further we will consider mooring effect to more realistically evaluate the performance of the proposed device in Section 3.2. In Section 3.3, a comprehensive evaluation on the influence of various design parameters on the SF-OSWEC performance is given. The dimensions of the SF-OSWEC and their initial values are shown in Fig. 2 and Table 1. The governing equations are solved with 4th-order Runge-Kutta method. For tidiness of flap density values, the water density is rounded to  $1000 \, \mathrm{kg/m^3}$  in the following.

#### 3.1. Comparison with traditional BH-FOSWEC

The boundary element mesh and calculated hydrodynamic parameters of SF-OSWEC and BH-FOSWEC are shown in Fig. 3 (calculated by NEMOH [47]). Subfigures (a) and (e) are the meshes for SF-OSWEC and BH-FOSWEC respectively (mesh convergence checked). For SF-OSWEC, the dimensions of both flaps are  $10~\text{m}\times5~\text{m}\times2~\text{m}$ ; For BH-FOSWEC, the dimensions are  $10~\text{m}\times10~\text{m}\times2~\text{m}$ . Subfigure (b) shows the radiation damping coefficients and the excitation force coefficients of surge, heave, and pitch motions of the top flap. The density of the top flap is  $500~\text{kg/m}^3$ . Subfigures (c) and (d) show those of the bottom flap and the coupling between the two flaps. The bottom flap has a density of  $1500~\text{kg/m}^3$ . Subfigure (f) shows the hydrodynamic parameters of the single flap device, whose density is  $500~\text{kg/m}^3$ .

A motion illustration of these two configuration is given in Fig. 4. The incident wave period is 10 s. Wave height is 1 m. The water condition is deep water. The PTO damping coefficient is  $1 \times$ 10<sup>6</sup> Nms/rad. The power production, the vertical reaction forces, and the motions of the two devices are compared in subfigures (a), (b), and (c) respectively. Note that to achieve fast stabilization of the motions, a 40 s ramp period is adopted at the beginning of the calculation. From subfigure (c), it is clear that the top and bottom flaps of SF-OSWEC rotates in opposite phases. In such case, the PTO rotation speed is the summation of these two speeds, and from subfigure (b), such self-balancing feature results in a significantly reduced reaction force on the foundation, which would lead to less reliability problems in engineering practice (although hard to quantify in this paper). Subfigures (d) and (e) shows the motions of the two devices in one cycle. Again subfigure (d) clearly shows the motion of the two flaps of SF-OSWEC in opposite phases. Please note that the damping  $1 \times 10^6$  Nms/rad here is not the optimal value for either SF-OSWEC or BH-FOSWEC. In the following we comprehensively evaluate the power performance of SF-OSWEC and BH-FOSWEC, with damping coefficients optimized for both systems.

The power generation spectrum with different PTO damping coefficients and under different incident wave periods are shown in Fig. 5. The power generation peak for SF-OSWEC happens at 9.5 s and  $1 \times 10^5$  Nms. For BH-FOSWEC, the peak is at 12.5 s and the optimal PTO damping is an order higher. Fig. 6 shows the maximized powers, capture width ratios, and corresponding optimal PTO damping coefficients of the two devices under different wave periods. The peak power output of BH-FOSWEC is higher than that of SF-OSWEC however SF-OSWEC has a larger peak capture width ratio. The optimal PTO damping coefficient of BH-FOSWEC is almost always larger than that of SF-OSWEC. Fig. 7 shows the phase difference between the motion of the two flaps of SF-OSWEC in different conditions. In the  $-200^{\circ} \sim -160^{\circ}$  region, the two flaps almost oscillate exactly in opposite phases; In the  $-220^{\circ} \sim -140^{\circ}$ region, although the motion is not exactly opposite, the phase difference still results in a rotation speed summation effect. These two regions add up to a major parameter space where the proposed

**Table 1**The simulation parameters of SF-OSWEC.

parameter	quantity
top flap density	$500 \text{ kg/m}^3$
bottom flap density	$1500 \text{ kg/m}^3$
flap height	5 m
flap thickness	2 m
flap width	10 m
top flap submerged depth	1 m

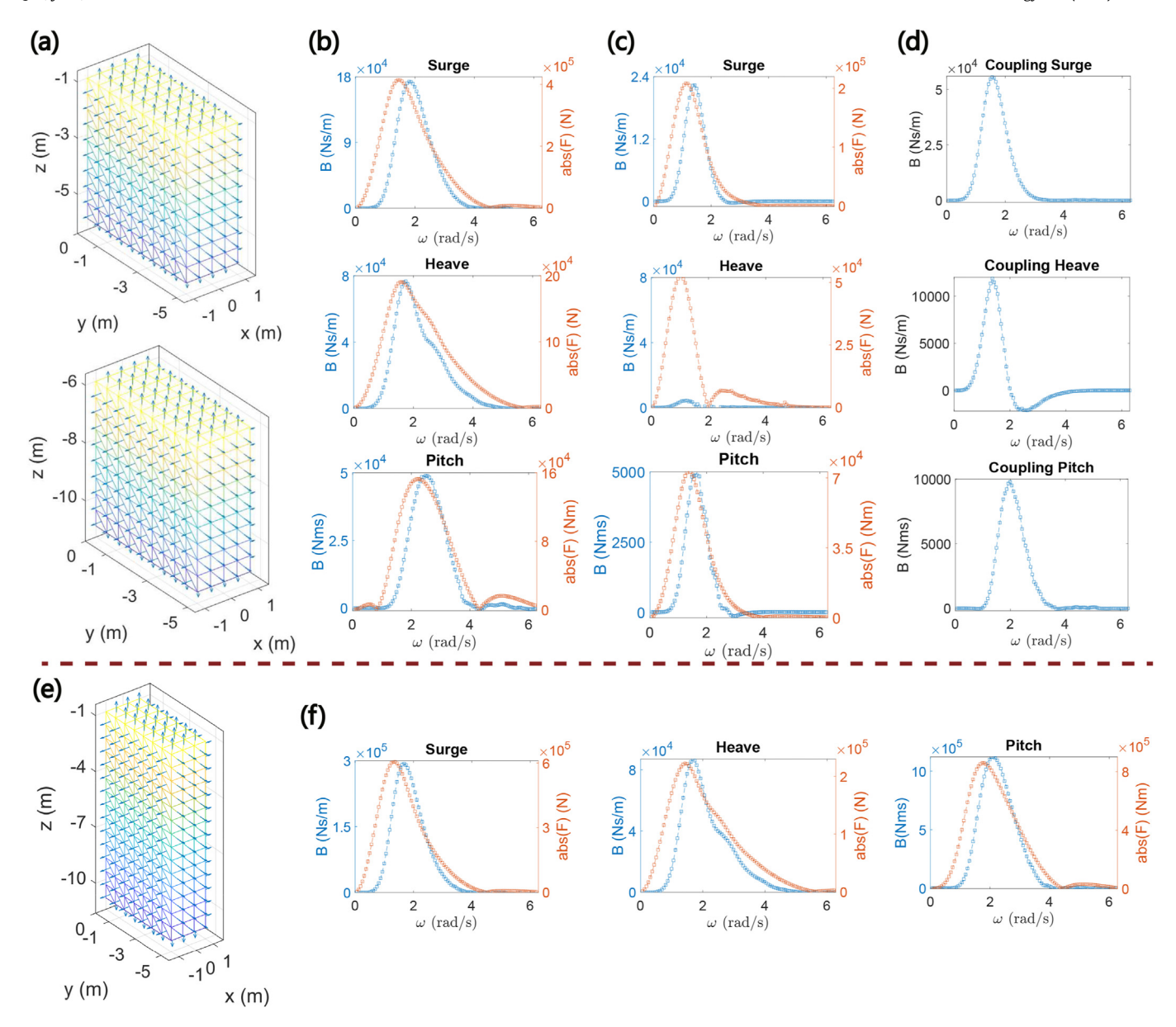


**Fig. 3.** The boundary element mesh and hydrodynamic parameters of the proposed SF-OSWEC and the compared BH-FOSWEC. (a) The boundary element meshes of the top and bottom flaps of SF-OSWEC; (b) The radiation damping coefficients and excitation force coefficients of the surge, heave, and pitch motions of the top flap; (c) The hydrodynamic parameters of the bottom flap; (d) The hydrodynamic parameters for the coupling of surge, heave, and pitch motions between the two flaps; (e) The boundary element mesh of BH-FOSWEC; (f) The hydrodynamic parameters of the BH-FOSWEC flap.

self-floating concept works. However, as indicated by the  $-20^{\circ} \sim 20^{\circ}$  region, if the PTO damping coefficient is excessively large, any significant relative motion between the two flaps is suppressed, i.e., the two flaps will be rotating in synchronized phases and the output energy will be minimized. Please note that the PTO damping can be conveniently realized with hydraulic PTOs or mechanical PTOs with multi-stage-amplification mechanisms [19,20], and tuned to optimal values, for example, by adjusting the resistance of the external circuit if a generator serves as the PTO.

## 3.2. The influence of moorings

In this section, moorings are considered in the system model (Eq. (18)) to verify the working principle of the SF-OSWEC in existence of mooring lines. However, limitations do exist since moorings are considered as springs and their inertia effect is

ignored. It should also be noted that in practice a frame is required to hold the PTO in the BH-FOSWEC configuration. However to simplify the modelling and comparison, the frame is ignored. It is also assumed that taut mooring configuration is adopted, since slack mooring configuration (catenary lines) permits relatively large surge motion, which is not desired for OSWECs. The mooring lines are installed with an inclination angle of 45° with respect to the seabed. We assume the horizontal and vertical stiffness coefficients of the moorings are the same. Two levels of horizontal stiffness are considered: 10<sup>7</sup> N/m and 10<sup>8</sup> N/m. The maximized power curves are shown in Fig. 8. For both mooring stiffness, the maximized power output curves of SF-OSWEC and BH-FOSWEC are similar to those under fixed-hinge condition. So the proposed contra-rotation mechanism works in existence of moorings. The vertical mooring forces of SF-OSWEC and BH-FOSWEC at their respective maximal power output points are compared in Fig. 9. In

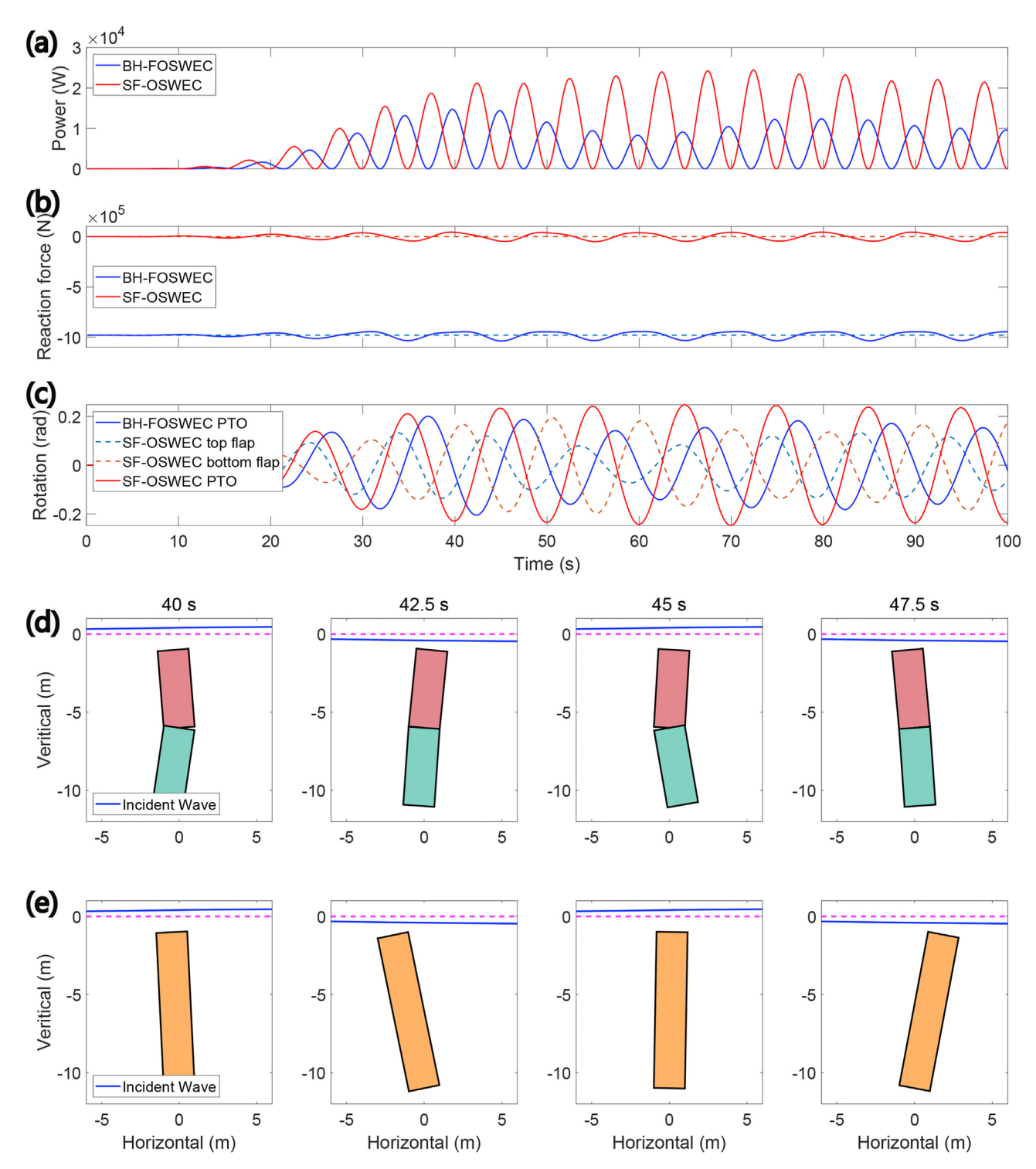


**Fig. 4.** Comparison between SF-OSWEC and BH-FOSWEC. Incident wave period and height are 10 s and 1 m. The PTO damping coefficient is  $1 \times 10^6$  Nms/rad (Note that this is not the optimal value for either system). (a) The instantaneous power output of SF-OSWEC and BH-FOSWEC; (b) The reaction force in the vertical direction of the two devices; (c) The rotation time histories of the two flaps of SF-OSWEC and of the BH-FOSWEC flap (=BH-FOSWEC PTO). The SF-OSWEC PTO rotation is the summation of those of the two flaps; (d) Illustration of the motion of SF-OSWEC in one cycle; (e) Illustration of the motion of SF-OSWEC in one cycle.

the steady state, the variation (maximum value - minimum value) of the mooring force of BH-FOSWEC is 25.4% larger than that of SF-OSWEC; the maximum absolute value of the mooring force of BH-FOSWEC is 5.17 times that of SF-OSWEC.

It should be noted that the peak period of BH-FOSWEC can be tuned lower if its averaged density is designed smaller, e.g. to  $9\ s$ 

with a density of 100 kg/m³. The power of BH-FOSWEC, in such cases, will be higher than SF-OSWEC (with a top flap density 500 kg/m³) at 9 s wave period. However, SF-OSWEC still possesses its unique advantages: (1) the reaction forces on mooring lines remains significantly smaller, especially when BH-FOSWEC has an extremely low density; (2) the density of the top flap of SF-OSWEC

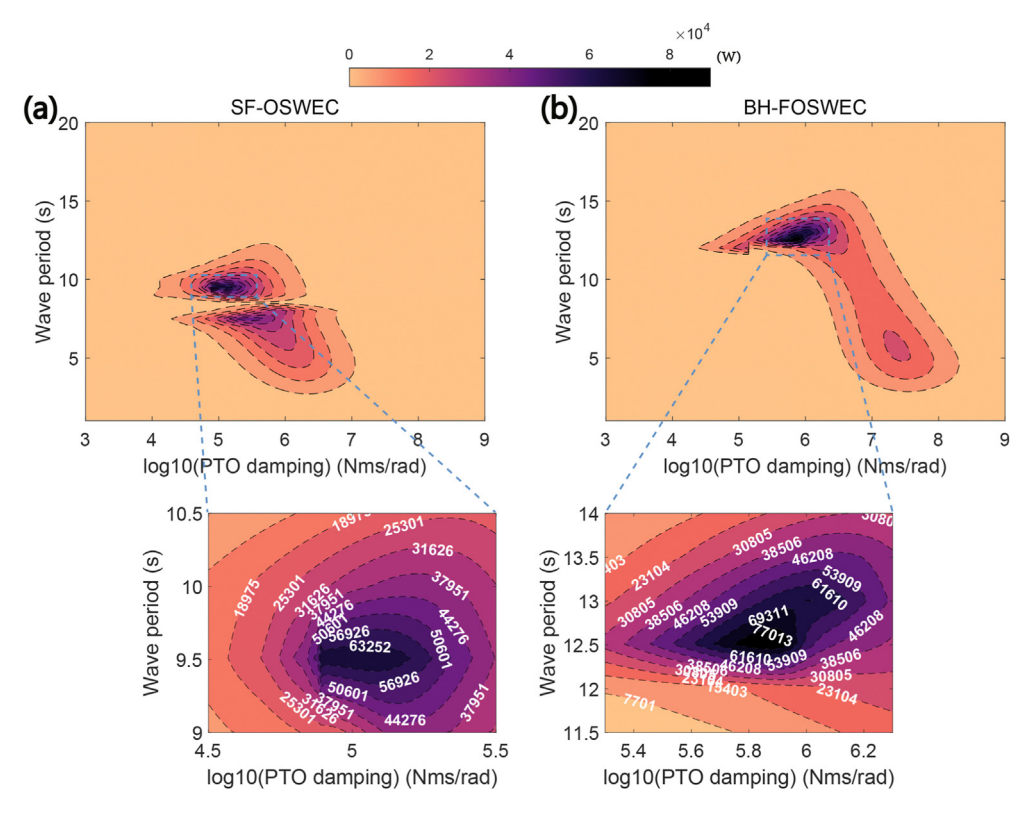


Fig. 5. The power generation spectrum (W) of the proposed SF-OSWEC and the compared BH-FOSWEC under regular wave excitation. Wave height is 1 m. (a) The SF-OSWEC power spectrum; (b) The BH-FOSWEC power spectrum.

can also be designed smaller for wave conditions where energy is concentrated around periods as low as 6 s-8 s.

The performance of two devices under irregular wave conditions are also studied. We use the Bretschneider Spectrum to generate the irregular waves. The maximized power output and capture width ratio under different peak periods are shown in Fig. 10. The significant wave height is kept 1m. The motion of two devices are calculated for 5000 s under each wave state. The power output is the averaged value of the last 4960 s since we adopted 40 s ramp at the beginning. From Fig. 10, between 5 s to 10 s peak periods, SF-OSWEC outperforms BH-FOSWEC; Above 10 s peak period, BH-FOSWEC has a higher power output. The 5000 s time histories under 7.5 s peak period wave are shown in Fig. 11. The enlarged view of the rotation displacements and speeds of the SF-OSWEC between 750 s and 850 s is shown in Fig. 12. In the majority of time, the PTO speed of SF-OSWEC adds up the speeds of the two flaps, and the power output is larger than that of BH-FOSWEC. This is also shown in the absorbed energy curves in Fig. 12 (b). Due to the self-floating property, the mooring force of SF-OSWEC remains smaller than that of BH-FOSWEC.

#### 3.3. The influence of other design parameters

In this section, we study the performance of SF-OSWEC in irregular waves under a range of design parameters and wave conditions, such as flap height, width, density, submerged depth, incident wave direction, and water depth. Please refer to Fig. 2 for the meaning of these design parameters. The horizontal and vertical mooring stiffness for the following cases is all set  $10^8~\text{N}/\text{m}$ . The irregular wave spectrum is still the Bretschneider spectrum. The significant wave height is kept 1 m. The submerged depth is kept 1 m in the following sections apart from Section 3.3.4.

#### 3.3.1. Flap height

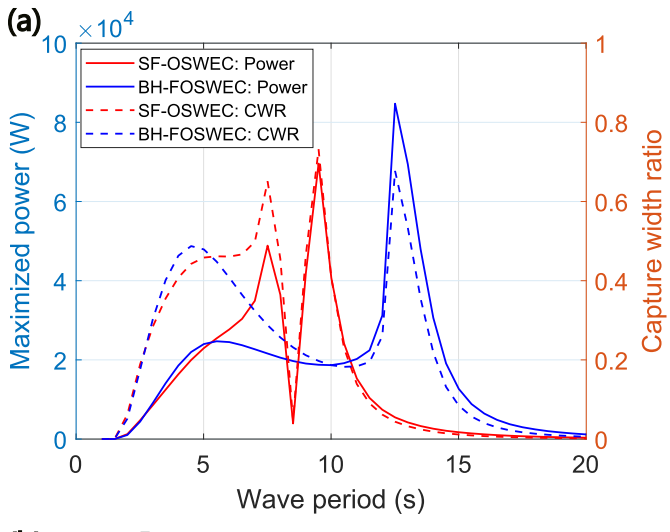
This section studies the influence of flap heights on the performance of SF-OSWEC. The considered values are 3 m, 5 m, 7 m, and 10 m. The optimal power curves are shown in Fig. 13. As the flap height increases, the rotational inertia of the flaps increases by the power of 3 while the restoring buoyancy or gravity moments increase by the power of 2, so the system natural periods will increase, as indicated in Fig. 13. However the maximum power output basically remains the same for different flap heights.

#### 3.3.2. Flap width

The influence of flap widths on the performance of SF-OSWEC is studied and shown in Fig. 14. The mass, inertia, and restoring buoyancy/gravity moments are all expected to grow linearly with respect to the increase of flap width. However due to the nonlinear change in hydrodynamic properties of the structure, the peak period of the maximum power output points of different flap heights does not remain exactly the same, which is a phenomenon also observed in Ref. [48]. However, the maximum power output values increase roughly linearly with respect to the flap width.

## 3.3.3. Flap density

This section studies the influence of flap densities on the performance of SF-OSWEC (see Fig. 15). The chosen densities of the top flap are  $400 \text{ kg/m}^3$ ,  $500 \text{ kg/m}^3$ ,  $700 \text{ kg/m}^3$ , and  $900 \text{ kg/m}^3$ . To keep the system self-floating under static states, the respective densities of the bottom flap are  $1600 \text{ kg/m}^3$ ,  $1500 \text{ kg/m}^3$ ,  $1300 \text{ kg/m}^3$ , and  $1100 \text{ kg/m}^3$ . Since the structure dimensions remain the same, the hydrodynamic properties such as radiation damping and added mass remain unchanged for all density cases. The variation of flap densities will change the flap mass/inertia properties and the restoring moments. The combination of these



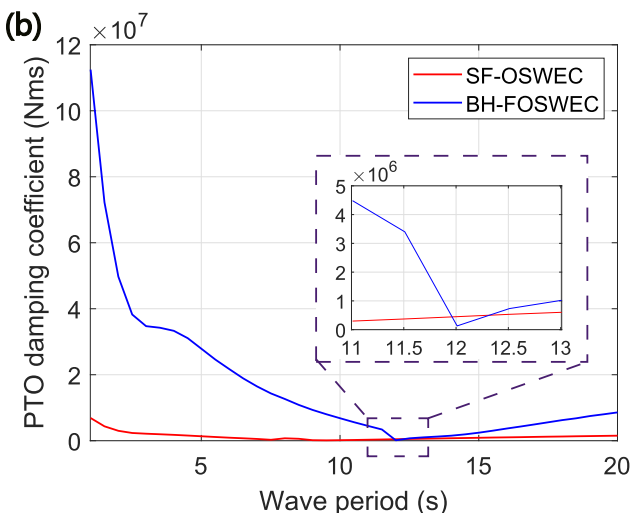


**Fig. 6.** (a) The maximized power and capture width ratio of SF-OSWEC and BH-FOSWEC with optimal PTO damping coefficients; (b) The optimal damping coefficients of the two devices under different incident wave periods.

facts results in the significant shifts of the system natural periods and characteristics of the power output curves. For 400 kg/  $m^3$  and 500 kg/ $m^3$  cases, the periods of maximum power output points are relatively small. Two peaks exist in the curve of 700 kg/  $m^3$ . The first peak is contributed by large hydrodynamic loading while the second one originates from the large resonance motion. As the density further increases to 900 kg/ $m^3$ , the second peak disappears since the natural period becomes too large and the hydrodynamic loading at this period is too small.

#### 3.3.4. Submerged depth

The influence of submerged depth on the performance of SF-OSWEC is studied and shown in Fig. 16. As expected, the increase of submerged depth will not change the natural period of the SF-OSWEC but will decrease the power output due to the decrease of power flux at larger submerged depth.

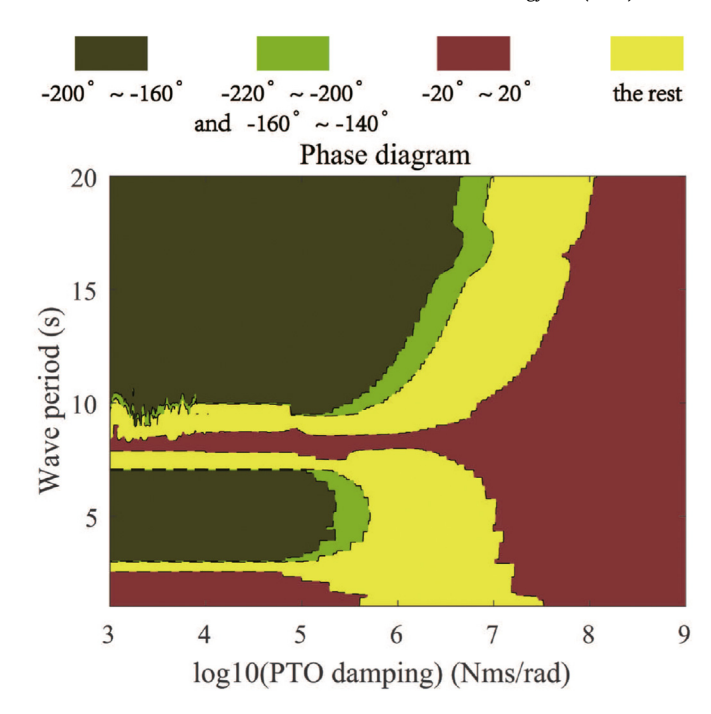


**Fig. 7.** The diagram of the phase difference between the motion of the two flaps of SF-OSWEC.

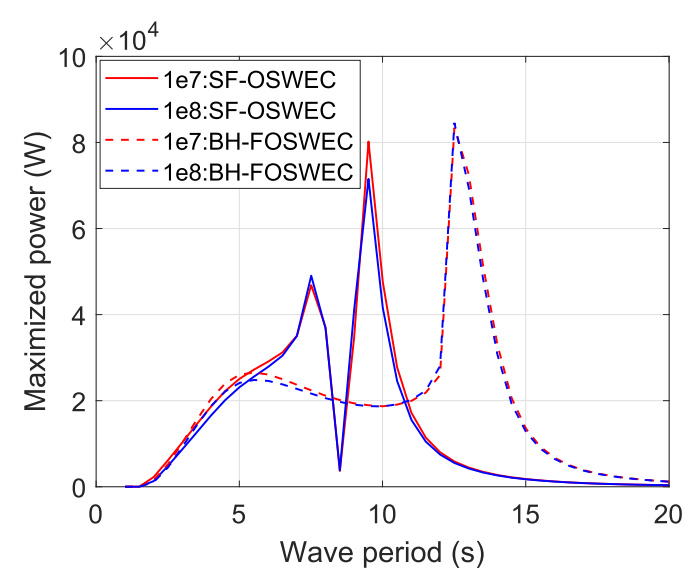
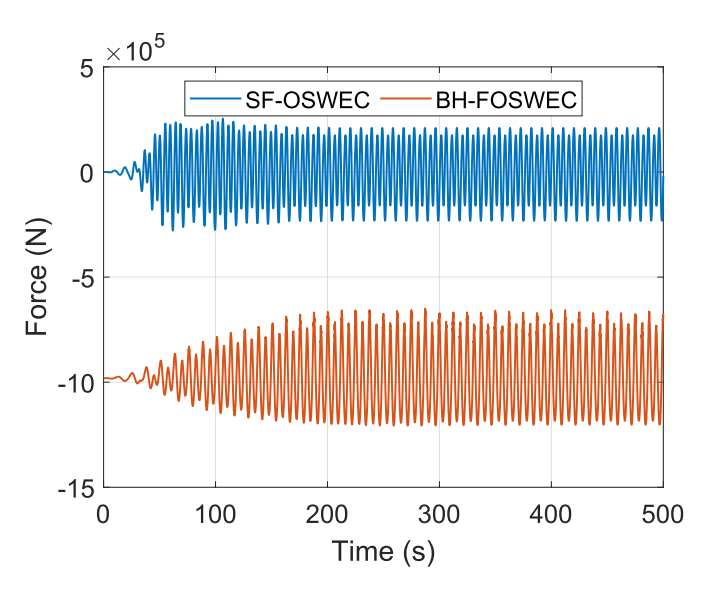


Fig. 8. The maximized powers of SF-OSWEC and BH-FOSWEC with different mooring stiffness. The two horizontal stiffness values are  $10^7~N/m$  and  $10^8~N/m$ .

## 3.3.5. Incident wave direction

The influence of incident wave directions on the performance of SF-OSWEC at 10 s and 15 s peak periods is shown in Fig. 17. Since the device is symmetrical with respect to the XOZ and YOZ planes, only the performances in the  $0^{\circ} \sim 90^{\circ}$  need to be calculated. The performances with respect to the other 3 quadrants can be symmetrically mapped. Since the device is supposed to rotate with respect to the Y axis, i.e., the roll motion is constrained, the power



**Fig. 9.** The vertical mooring force histories of SF-OSWEC and BH-FOSWEC at their respective optimal regular wave states.

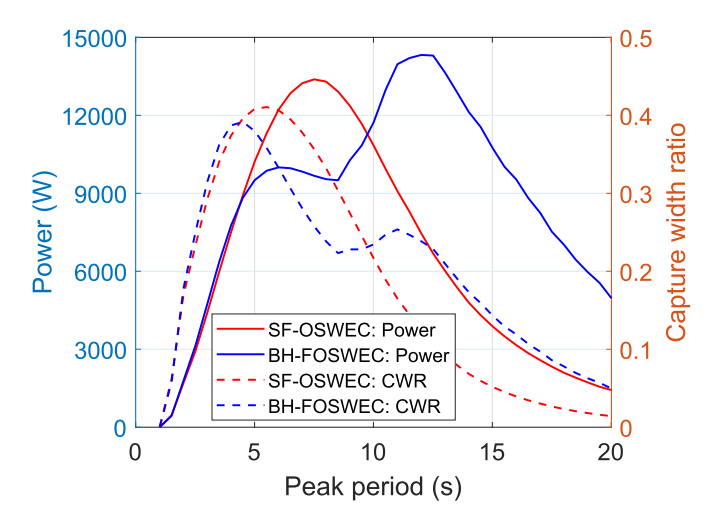


**Fig. 10.** The maximized power output and capture width ratio of SF-OSWEC and BH-FOSWEC under irregular wave conditions.

output with 90° incident wave is 0. The trend is as expected: the power output is larger when the incident wave direction is more parallel to 0°. However due to the finite dimension of the device, the output power is not exactly following a cosine relationship with respect to the direction angles. One rough estimation is that if the incident wave direction is within the  $-30^{\circ} \sim 30^{\circ}$  range, the power output drop is less than 30%.

The results suggest that SF-OSWEC is suited for nearshore applications since waves are generally normal to the shoreline. In deep water, the oblique waves will induce yaw motion of the system and reduce the power output. However, deep water applications are still favoured [43] because of the unique self-balancing feature of SF-OSWEC, the permitting and regulation issues at near

shore sites [49], and the superior wave resources in deep water [50].

#### 3.3.6. Water depth

This section studies the influence of the water depth on the performance of SF-OSWEC. The considered water depth values are 12 m, 20 m, 40 m, and infinite depth (deep water condition). The submerged depth and wave height are both kept 1 m. The flap dimensions are the same as in Table 1. As shown in Fig. 18, the generated power increases as the water depth decreases. For deep water conditions, the fluid motion, thus the energy, is distributed along the water depth, especially for large period waves. As a result, when the wave height is the same, the flaps are subject to larger excitation forces in shallow water than in deep water.

#### 4. Conclusions

In this paper, we propose a new configuration for oscillating surge wave energy converters (OSWECs), named self-floating OSWEC (SF-OSWEC). The SF-OSWEC is consisted of two vertically placed flaps with a common hinge. The top flap is lighter than water while the bottom one is denser. When driven by incident waves, the two flaps will oscillate in opposite directions and phases. Kinetic energy can be extracted from the relative motion between the two flaps by a power take-off (PTO) system at the hinge, such as a generator whose rotor and stator are connected with each of the flaps. We have conducted a thorough numerical study on the performance of SF-OSWEC, as well as its comparison to a bottomhinged floating OSWEC (BH-FOSWEC) of the same overall dimensions. Results have shown that the opposite-rotation mechanism works under incident waves of different periods as long as the PTO damping is appropriately tuned, no matter whether the hinge is fixed or connected with mooring lines. Generally the resonant period and optimal PTO damping of a SF-OSWEC are smaller than those of a BH-FOSWEC of the same overall dimensions. However, the peak capture width ratio is higher. Another advantage of the SF-OSWEC is that it imposes a significantly smaller loading on the mooring lines compared with the BH-FOSWEC, which can potentially reduce the material and manufacturing costs on mooring lines and increase the reliability of the device in deep ocean conditions. Further, with the opposite-rotation mechanism, SF-OSWEC can get rid of the supporting frame commonly required to hold the PTO in the BH-FOSWEC configuration. Under irregular wave excitation, the two flaps of SF-OSWEC oscillate in opposite directions in the majority of the time, although not all the time due to the inclusion of multiple frequency components. The influence of flap height, width, density, submerged depth, incident wave direction, and water depth on the performance and dynamic properties of SF-OSWEC is also studied in detail. Overall the SF-OSWEC is a promising concept for various applications such as ocean observation, utility electricity, marine aquaculture, coastline protection, and seawater desalination in deep ocean conditions.

### **Author contribution**

Qiaofeng Li: Conceptualization, Methodology, Software, Writing – original draft; Jia Mi: Validation, Writing – review & editing, Visualization; Xiaofan Li: Validation, Writing – review & editing,

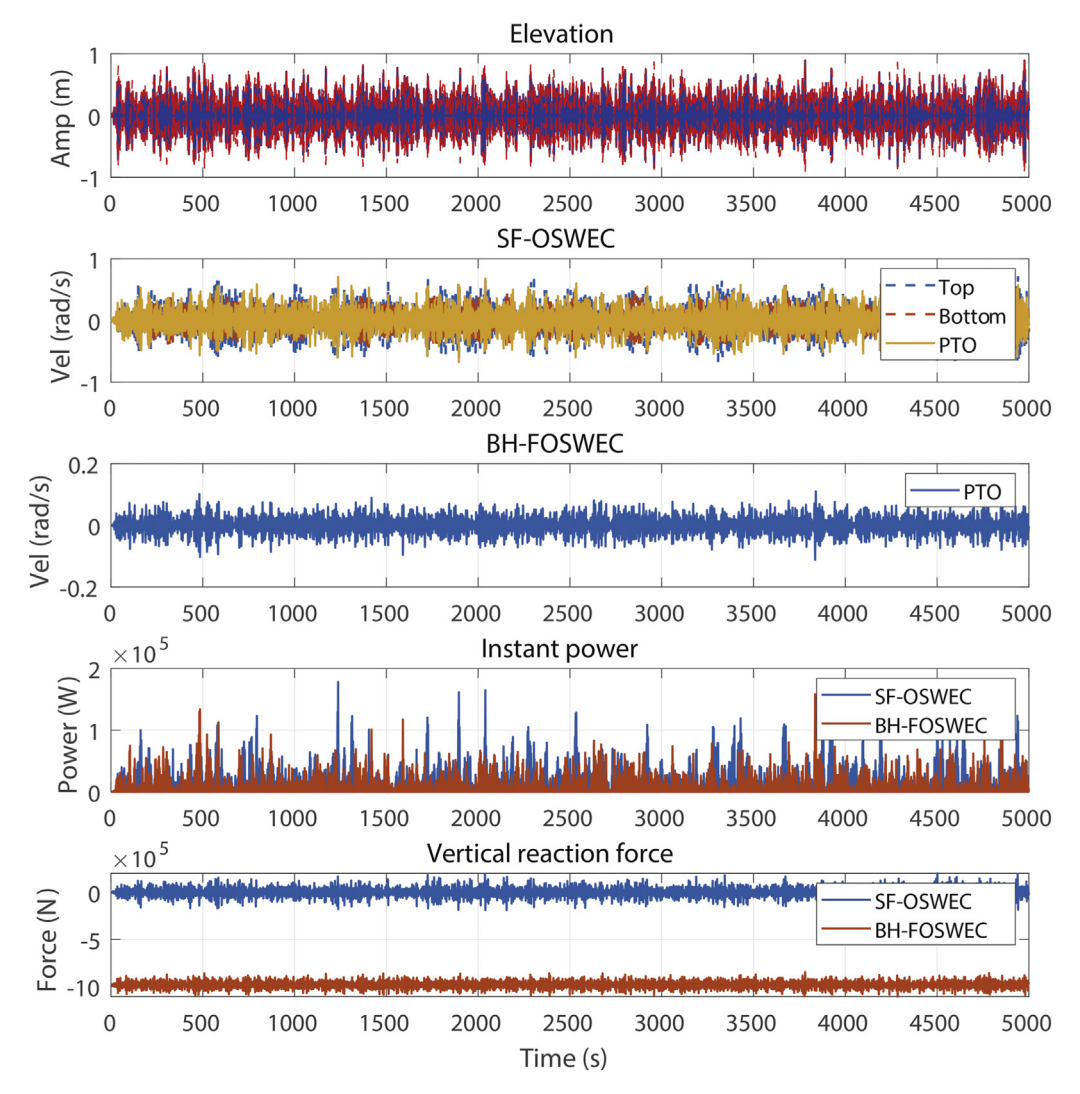


**Fig. 11.** Comparison of motion, power output, and mooring line reaction force of SF-OSWEC and BH-FOSWEC under 7.5 s irregular wave. The time histories are synchronized with wave elevation series in the top row. In most time, the proposed contra-rotation mechanism results in a speed addition effect (i.e., the PTO speed constitutes the envelope), and the power output of SF-OSWEC is larger. This is achieved with a smaller force imposed on the mooring lines, as shown in the bottom row.

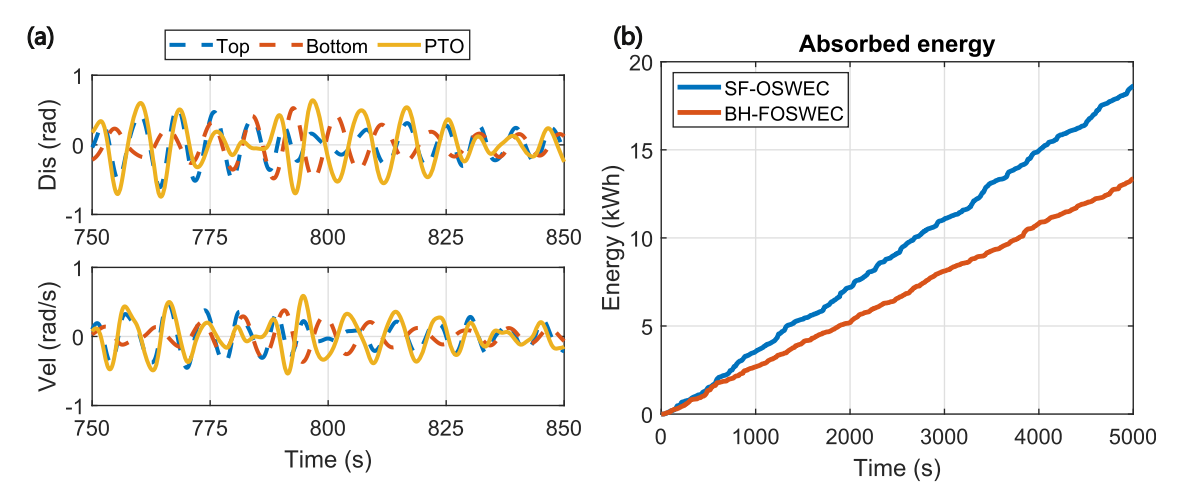
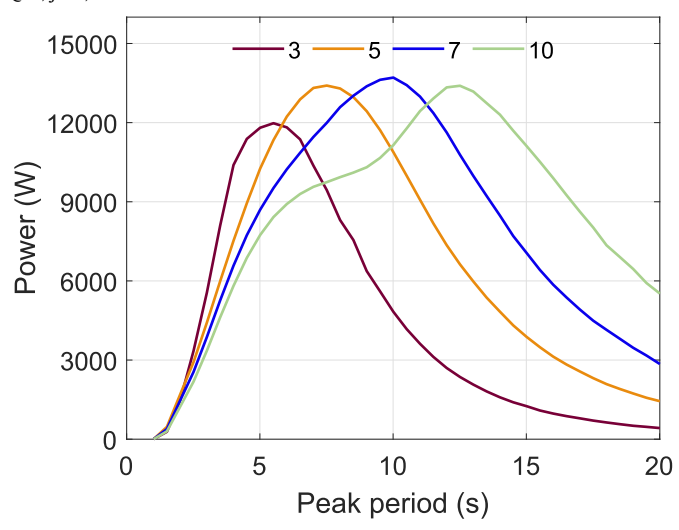
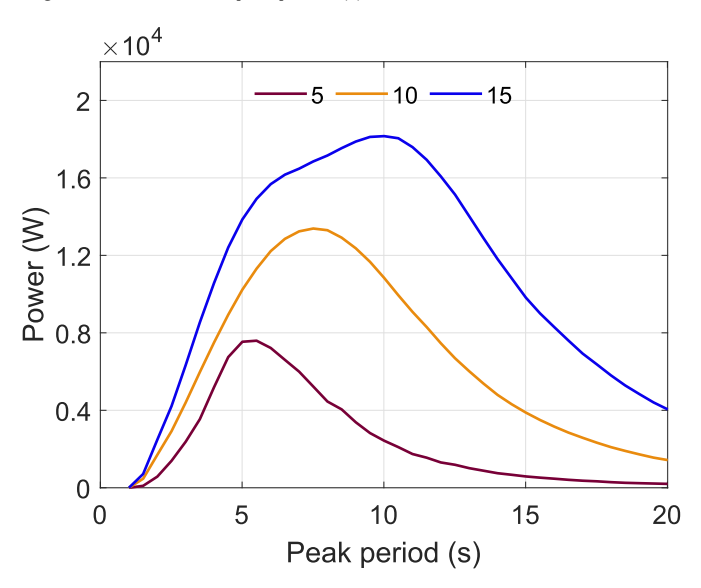


Fig. 12. (a) The enlarged view of the rotation displacements and speeds of the SF-OSWEC between 750 s and 850 s under 7.5 s peak period 1 m wave height irregular wave excitation; (b) The comparison of absorbed energy between SF-OSWEC and BH-FOSWEC.



**Fig. 13.** The power output (W) of the SF-OSWEC with different flap heights (m) under irregular waves of different peak periods (s).



 $\begin{tabular}{ll} Fig. 14. The power output (W) of the SF-OSWEC with different flap widths (m) under irregular waves of different peak periods (s). \end{tabular}$ 

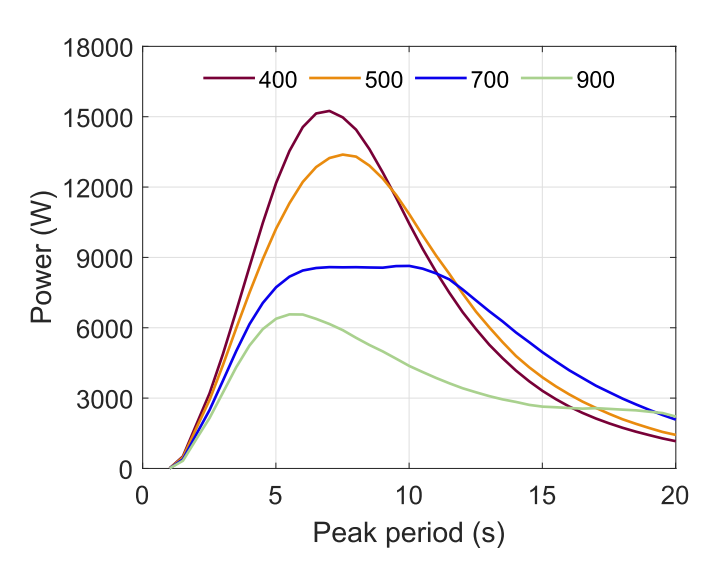
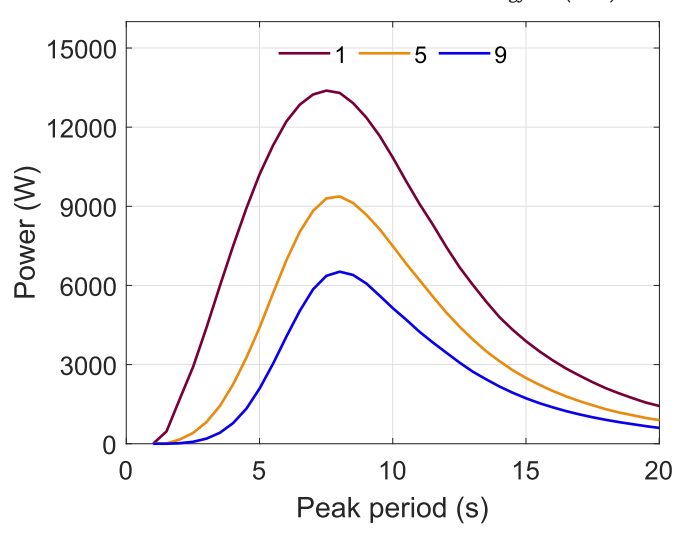
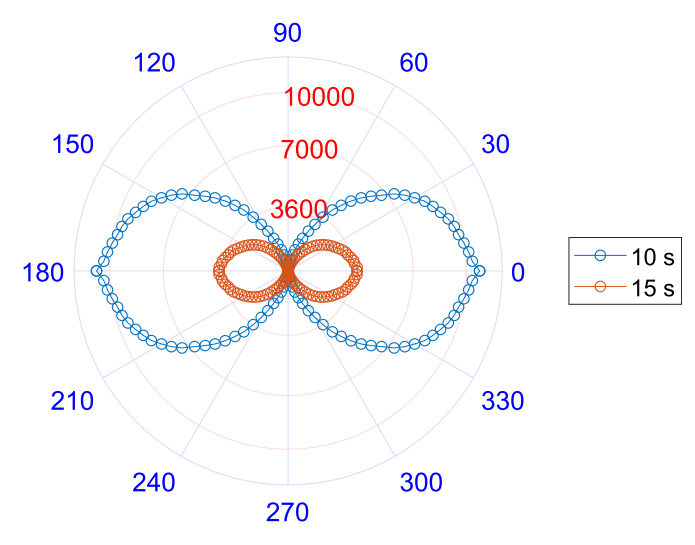


Fig. 15. The power output (W) of the SF-OSWEC with different flap densities (kg/  $m^3$ ) under irregular waves of different peak periods (s).



 $\begin{tabular}{ll} \textbf{Fig. 16.} & The power output (W) of the SF-OSWEC with different submerged depth (m) under irregular waves of different peak periods (s). \end{tabular}$ 



**Fig. 17.** The power output (W) of the SF-OSWEC with different incident wave directions (deg) at peak periods of  $10 \, \text{s}$  and  $15 \, \text{s}$ .

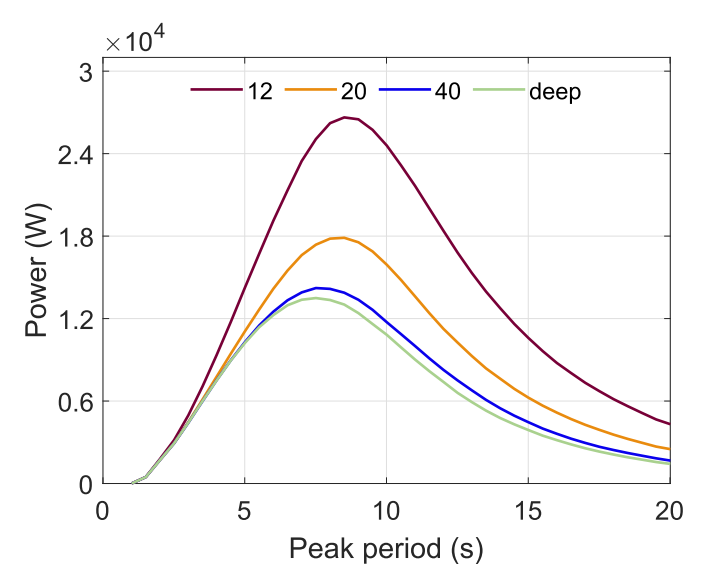


**Fig. 18.** The power output (W) of the SF-OSWEC with different water depth (m) under irregular waves of different peak periods (s).

Visualization; Shuo Chen: Validation; Boxi Jiang: Validation; Lei Zuo: Resources, Writing — review & editing, Supervision, Project administration, Funding acquisition

#### **Declaration of competing interest**

The authors declare that they have no known competing financial interests or personal relationships that could have appeared to influence the work reported in this paper.

#### Acknowledgement

This material is based upon work supported by the U.S. Department of Energy's Office of Energy Efficiency and Renewable Energy (EERE) under the Water Power Technologies Office Award Number DE-EE0007174 and the National Science Foundation under Grant No. 1903627.

#### References

- [1] IEA-OES annual report, tech. Rep. International Energy Agency, Ocean Energy Systems; 2007.
- [2] Czech B, Bauer P. Wave energy converter concepts: design challenges and classification. IEEE Industrial Electronics Magazine 2012;6(2):4–16.
- [3] Falcão AFdO. Wave energy utilization: a review of the technologies. Renew Sustain Energy Rev 2010;14(3):899–918.
- [4] Wave energy road map, tech. Rep. Supergen ORE Hub; 2020.
- [5] Folley M, Suarez BP, Whittaker T. An autonomous wave-powered desalination system. Desalination 2008;220:412–21.
- [6] Brito-Melo A, Gato L, Sarmento A. Analysis of wells turbine design parameters by numerical simulation of the owc performance. Ocean Eng 2002;29: 1463-77
- [7] Boccotti P. Design of breakwater for conversion of wave energy into electrical energy. Ocean Eng 2012;51:106–18.
- [8] Henriques JCC, Gato LMC, Falcão AFO, Robles E, Faÿ FX. Latching control of a floating oscillating-water-column wave energy converter. Renew Energy 2016;90:229–41.
- [9] Elhanafi A, Macfarlane G, Fleming A, Leong Z. Experimental and numerical investigations on the hydrodynamic performance of a floating—moored oscillating water column wave energy converter. Appl Energy 2017;205: 260, 00
- [10] Hur DS, Jeong YM, Lee JL, Kim IH, Lee WD. Energy generation efficiency due to wave overtopping on floating-overflow-type wave energy converter. J Coast Res 2018;85:1341-5.
- [11] Vicinanza D, Contestabile P, Quvang Harck Nørgaard J, Lykke Andersen T. Innovative rubble mound breakwaters for overtopping wave energy conversion. Coast Eng 2014;88:154–70.
- [12] Babarit A. A database of capture width ratio of wave energy converters. Renew Energy 2015;80:610—28.
- [13] Henderson R. Design, simulation, and testing of a novel hydraulic power takeoff system for the pelamis wave energy converter. Renew Energy 2006;31(2): 271–83
- [14] Stansby P, Carpintero Moreno E, Stallard T. Large capacity multi-float configurations for the wave energy converter m4 using a time-domain linear diffraction model. Appl Ocean Res 2017;68:53–64.
- [15] Carpintero Moreno E, Stansby P. The 6-float wave energy converter m4: ocean basin tests giving capture width, response and energy yield for several sites. Renew Sustain Energy Rev 2019;104:307–18.
- [16] Liao Z, Gai N, Stansby P, Li G. Linear non-causal optimal control of an attenuator type wave energy converter m4. IEEE Transactions on Sustainable Energy 2020;11(3):1278–86.
- [17] Beatty SJ, Hall M, Buckham BJ, Wild P, Bocking B. Experimental and numerical comparisons of self-reacting point absorber wave energy converters in regular waves. Ocean Eng 2015;104:370–86.
- [18] Liang C, Ai J, Zuo L. Design, fabrication, simulation and testing of an ocean wave energy converter with mechanical motion rectifier. Ocean Eng 2017;136:190–200.
- [19] X. Li, C. Liang, C.-A. Chen, Q. Xiong, R. G. Parker, L. Zuo, Optimum power analysis of a self-reactive wave energy point absorber with mechanicallydriven power take-offs, Energy 195.
- [20] X. Li, C. Chen, Q. Li, L. Xu, C. Liang, K. Ngo, R. G. Parker, L. Zuo, A compact mechanical power take-off for wave energy converters: design, analysis, and test verification, Appl Energy 278.
- [21] Folley M, Whittaker TJT, Henry A. The effect of water depth on the

- performance of a small surging wave energy converter. Ocean Eng 2007;34(8–9):1265–74.
- [22] Gomes RPF, Lopes MFP, Henriques JCC, Gato LMC, Falcão AFO. The dynamics and power extraction of bottom-hinged plate wave energy converters in regular and irregular waves. Ocean Eng 2015;96:86–99.
- [23] Yu H-F, Zhang Y-L, Zheng S-M. Numerical study on the performance of a wave energy converter with three hinged bodies. Renew Energy 2016;99:1276–86.
- [24] Deng Z, Wang L, Zhao X, Wang P. Wave power extraction by a nearshore oscillating water column converter with a surging lip-wall. Renew Energy 2020;146:662–74.
- [25] Martin D, Li X, Chen C-A, Thiagarajan K, Ngo K, Parker R, Zuo L. Numerical analysis and wave tank validation on the optimal design of a two-body wave energy converter. Renew Energy 2020;145:632—41.
- [26] Younesian D, Alam M-R. Multi-stable mechanisms for high-efficiency and broadband ocean wave energy harvesting. Appl Energy 2017;197:292–302.
- [27] López M, Taveira-Pinto F, Rosa-Santos P. Influence of the power take-off characteristics on the performance of ceco wave energy converter. Energy 2017;120:686–97.
- [28] Jin S, Patton RJ, Guo B. Enhancement of wave energy absorption efficiency via geometry and power take-off damping tuning. Energy 2019;169:819–32.
- [29] X. Zhang, X. Tian, L. Xiao, X. Li, W. Lu, Mechanism and sensitivity for broad-band energy harvesting of an adaptive bistable point absorber wave energy converter, Energy 188.
- [30] Zhang H, Xi R, Xu D, Wang K, Shi Q, Zhao H, Wu B. Efficiency enhancement of a point wave energy converter with a magnetic bistable mechanism. Energy 2019;181:1152–65.
- [31] Tom N, Lawson M, Yu Y-H, Wright A. Spectral modeling of an oscillating surge wave energy converter with control surfaces. Appl Ocean Res 2016;56: 143–56.
- [32] Tom NM, Yu YH, Wright AD, Lawson MJ. Pseudo-spectral control of a novel oscillating surge wave energy converter in regular waves for power optimization including load reduction. Ocean Eng 2017;137:352–66.
- [33] Davidson J, Genest R, Ringwood JV. Adaptive control of a wave energy converter. IEEE Transactions on Sustainable Energy 2018;9(4):1588–95.
- [34] Burgaç A, Yavuz H. Fuzzy logic based hybrid type control implementation of a heaving wave energy converter. Energy 2019;170:1202–14.
- [35] Whittaker T, Folley M. Nearshore oscillating wave surge converters and the development of Oyster. Philos Trans A Math Phys Eng Sci 2012;370(1959): 345–64.
- [36] Maki T, Vuorinen M, Mucha T. Waveroller one of the leading technologies for wave energy conversion. Halifax, Canada: 5th International Conference on Ocean Energy; 2014.
- [37] Chehaze W, Chamoun D, Bou-Mosleh C, Rahme P. Wave roller device for power generation. Procedia Engineering 2016;145:144–50.
- [38] Ramudu E. Ocean wave energy-driven desalination systems for off-grid coastal communities in developing countries. In: 2011 IEEE global humanitarian technology conference; 2011. p. 287–9.
- [39] Reavis C, Zuckerman E. Resolute marine energy: power in waves. 2014.
- [40] Sarkar D, Doherty K, Dias F. The modular concept of the oscillating wave surge converter. Renew Energy 2016;85:484–97.
- [41] Tom NM, Lawson MJ, Yu YH, Wright AD. Development of a nearshore oscillating surge wave energy converter with variable geometry. Renew Energy 2016;96:410–24.
- [42] K. Ruehl, D. D. Forbush, Y.-H. Yu, N. Tom, Experimental and numerical comparisons of a dual-flap floating oscillating surge wave energy converter in regular waves, Ocean Eng 196.
- [43] Yu Y, Jenne D, Thresher R, Copping A, Geerlofs S, Hanna L. Reference model 5 (RM5): oscillating surge wave energy converter, Tech. rep. Golden, CO (United States): National Renewable Energy Lab.(NREL); 2015.
- [44] Schmitt P, Bourdier S, Whittaker T, Sarkar D, Renzi E, Dias F, Doherty K, van't Hoff J, et al. Hydrodynamic loading on a bottom hinged oscillating wave surge converter. In: The twenty-second international offshore and polar engineering conference. International Society of Offshore and Polar Engineers; 2012.
- [45] Musial W, Lawson M, Rooney S. Marine and hydrokinetic technology (MHK) instrumentation, measurement, and computer modeling workshop, Tech. rep. Golden, CO (United States): National Renewable Energy Lab.(NREL); 2013.
- [46] Cummins W. The impulse response function and ship motions. Schiffstechnik 1962;47(9):101–9.
- [47] A. Babarit, G. Delhommeau, Theoretical and numerical aspects of the open source BEM solver NEMOH, in: Proc. Of the 11th European wave and tidal energy conference (EWTEC2015).
- [48] Henry A, Folley M, Whittaker T. A conceptual model of the hydrodynamics of an oscillating wave surge converter. Renew Energy 2018;118:965–72.
- [49] Copping AE, Geerlofs SH, Hanna LA. The contribution of environmental siting and permitting requirements to the cost of energy wave energy devices: reference model 5. Richland, WA (United States): Tech. rep., Pacific Northwest National Lab.(PNNL); 2014.
- [50] Babarit A, Hals J, Muliawan MJ, Kurniawan A, Moan T, Krokstad J. Numerical benchmarking study of a selection of wave energy converters. Renew Energy 2012;41:44–63.